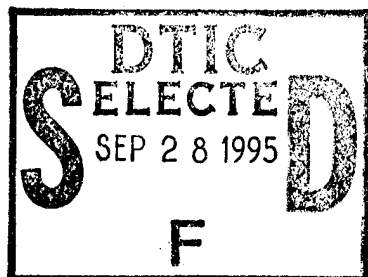


A Novel Technique for 4-Dimensional Atmosphere and Oceanographic Irradiance Measurements Using 3-D Spatial Filtering

Contract No. N00014-94-C-0099

Period of Performance: 04/14/94 to 09/30/94



Bi-Monthly Report

Reporting Period: 04/14/94 to 05/31/94

Presented to:

Office of Naval Research
Ballston Tower One
800 North Quincy Street
Arlington, VA 22217-5660

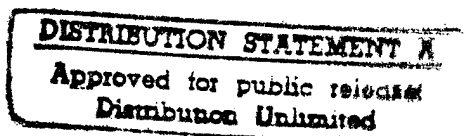
Scientific Officer:

Steve Ackleson

Presented by:

Physical Optics Corporation
Research and Development Division
20600 Gramercy Place, Suite 103
Torrance, California 90501

Accession For	
NTIS CRA&I	<input checked="checked" type="checkbox"/>
DTIC TAB	<input type="checkbox"/>
Unannounced	<input type="checkbox"/>
Justification	
By <i>per lti</i>	
Distribution /	
Availability Codes	
Dist	Avail and/or Special
<i>A-1</i>	



Principal Investigator:

Shudong Wu
(310) 320-3088

June 1994

19950925 176

Bi-Monthly 0594.3267 ONR-4D

~~94 7 19 120~~

In the first two months of the program, Physical Optics Corporation has analytically evaluated the depth discrimination performance of pixel filters. These studies indicate that pixel filters have good depth discrimination capability for an array of discrete point light sources. The discrimination contrast is about 20:1. We also evaluated the effects of imaging lens aberrations and wavelength variation. This report describes in detail the numerical evaluation.

1.0 MODELING THE IMAGING SYSTEM

As stated in the proposal, this imaging system can be described in terms of two diffractions. The geometry of the system is represented in Figure 1. The same symbols are used as in the proposal.

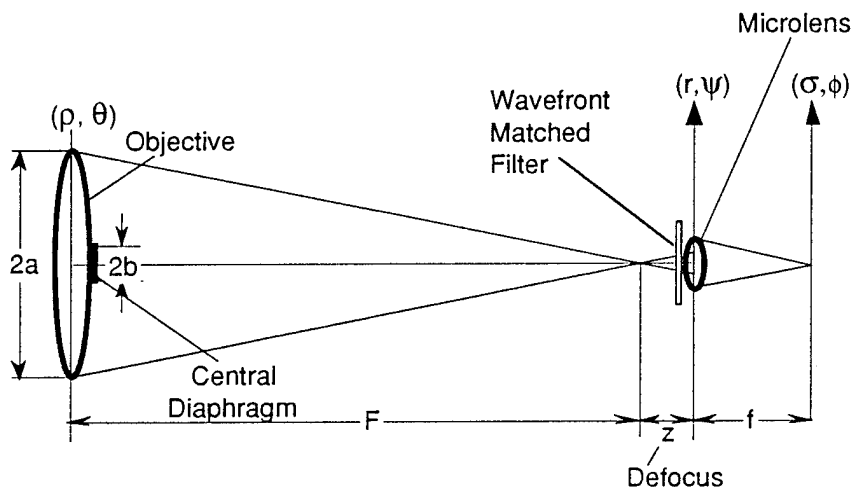


Figure 1
Geometry of the double diffraction in the system.

Suppose that a , b , c , and e are the radii of the objective lens, the central diaphragm, the microlenses and the pinholes, respectively; F and f are the imaging distance and the focal length of microlenses, respectively; z is the defocus distance. Finally, (ρ, θ) , (r, ψ) , and (σ, ϕ) are polar coordinate systems in the objective lens plane, microlens plane, and the output image plane, respectively. Let us define the following normalized coordinates:

$$u = \frac{2\pi}{\lambda} \left(\frac{a}{F} \right)^2 z \quad (1)$$

and

$$v = \frac{2\pi}{\lambda} \left(\frac{a}{F} \right) r \quad (2)$$

The optical field on the microlens array plane can be calculated by

$$W(u, v) = \int_{b/a}^1 J_0(v \cdot \rho) \exp\left(ju \frac{\rho^2}{2}\right) \rho d\rho, \quad (3)$$

where $J_0(x)$ is the zero order Bessel function. This is the optical field generated by a point source located at the axial point of the object plane.

In order to simplify the calculations, we first calculated the defocus response for a point source array on the object plane. The point source separation is equal to the diameter of the microlens, c . Further, we assumed that the point source array is arranged in a circular symmetry as shown in Figure 2. The M -th ring of point sources is on a circle with a radius equal to Mc . All point sources contribute energy to the pinhole on the axis shown in Figure 1. We sum up the energy from all point sources to calculate the defocus response.

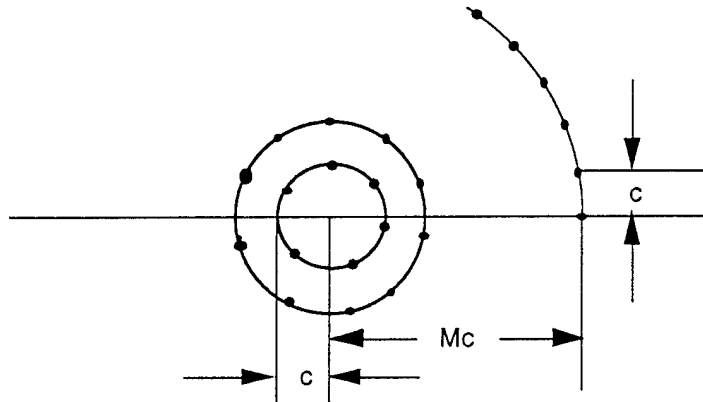


Figure 2
A point source array arranged in circular symmetry.

For the sake of convenient calculation, we calculated the energy summation in another way. Rather than assuming a point source array and single pixel filter, we equivalently used a pixel filter array and a single point source for the numerical calculation. Thus, we have a microlens array with

a pinhole array on the focal plane of the microlens array. The microlenses are arranged in the same way as the point sources shown in Figure 2. We calculated the field diffracted onto each microlens by the imaging lens, then calculated the field on the corresponding pinholes, and finally, summed the energy on all pinholes.

It is convenient to introduce a local coordinate system for each microlens and pinhole as shown in Figure 3.

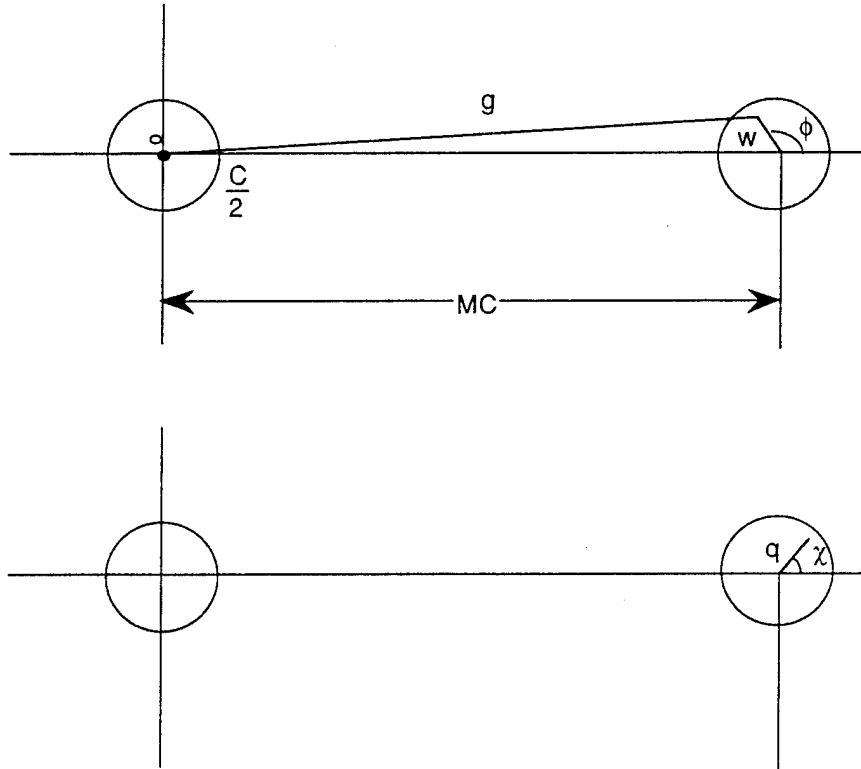


Figure 3
Local coordinate systems (w, ϕ) for the microlens plane and (q, χ) for the pinhole plane.

The fields on the M -th microlens can be expressed by Eq. (3) substituted by $\frac{2\pi}{\lambda} \left(\frac{a}{F} \right) g$, where g is given by

$$g = \sqrt{(2Mc + w \cos \phi)^2 + (w \sin \phi)^2} . \quad (4)$$

The field on the pinhole plane diffracted by the M -th microlens can be expressed by a Fourier transform in the polar coordinate system

$$G_M(u, q, \chi) = \int_0^{2\pi} d\phi \int_0^{C/2} W\left(u, \frac{2\pi}{\lambda} \left(\frac{a}{F}\right) g\right) \exp\left[-j \frac{(2\pi)^3}{\lambda} \left(\frac{a}{F}\right)^2 wq \cos(\phi - \chi)\right] \cdot w dw \quad (5)$$

To simplify the calculation, the field on the pinhole is considered to be uniform so that only the field at the center of the pinhole (that is, $q = 0$ in Eq. (5)) needs to be calculated. Thus, we can drop both q and χ in Eq. (5) so that

$$G_M(u) = \int_0^{2\pi} d\phi \int_0^{C/2} W\left(u, \frac{2\pi}{\lambda} \left(\frac{a}{F}\right) g\right) w dw \quad (6)$$

To sum up the energy at all pinholes, we only need to calculate the field intensity in the pinholes in one radial direction.

The total intensity from the pinholes on the M -th ring is estimated by multiplying the equivalent number of microlenses in a given ring by the intensity at the M -th pinhole. The equivalent number of microlenses on the M -th size is given by

$$2M\pi + \delta(M) \quad (7)$$

$$\text{where} \quad \delta(M) = \begin{cases} 1, & \text{for } M = 0, \\ 0, & \text{for } M \neq 0. \end{cases} \quad (8)$$

Thus, the energy summation can be expressed

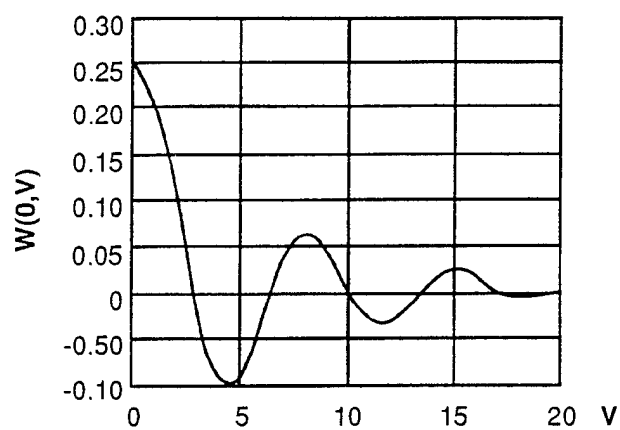
$$I(u) = \sum_{M=0}^{M_{\max}} |G_M(u)|^2 (2\pi M + \delta(M)) \quad (9)$$

Notice that $I(u)$ is a function of u , the normalized defocus distance (see Eq. (1)), representing the defocus response of the imaging system. If $I(u)$ is not dependent on u , it means that the system has no depth discrimination capability. If $I(u)$ is a function with a strong peak at $u = 0$, the system has strong depth discrimination capability. In the following sections, we use the formulas developed above to evaluate the depth discrimination capabilities for various situations.

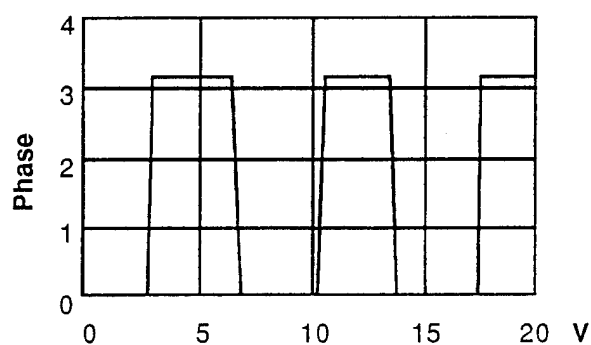
2.0 DEPTH DISCRIMINATION CAPABILITIES USING WAVEFRONT MATCHED FILTERS

Figure 5(a) shows the diffracted field on the microlens plane, calculated by Eq. (3) with the central obstruction ratio $b/a = 0.5$. It consists of a central spot and a few rings. If the microlens diameter is greater than the central spot size (Airy spot size), a π -phase wavefront matched filter is required to correct the negative phase of the pattern. The phase distribution of the filter is shown in Figure 5(b). Figure 5(c) shows the structure of the pixel filter. A microlens size equal to five times the Airy spot size was used. We calculated the defocus response of the pixel filter by Eqs. (1) to (9). The computation was very time-consuming -- it took three days to calculate one curve using a 486 personal computer. Figure 6 shows the calculated defocus response curve. It indicates a sharp depth discrimination capability and good contrast of about 50. In comparison, the defocus response curve for a conventional system is a flat horizontal line with no depth discrimination capability at all.

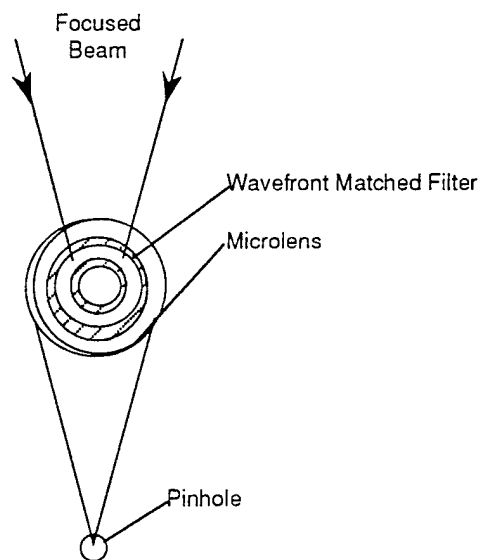
We also calculated the defocus response for various values of central obstruction ratio. Figure 7 shows the calculated curves. It indicates that there is no significant effect in the defocus response for various central stop sizes.



(a)



(b)



(c)

Figure 5

(a) Field amplitude distribution on the wavefront matched filter, (b) phase distribution of the wavefront matched filter, and (c) structure of a pixel filter.

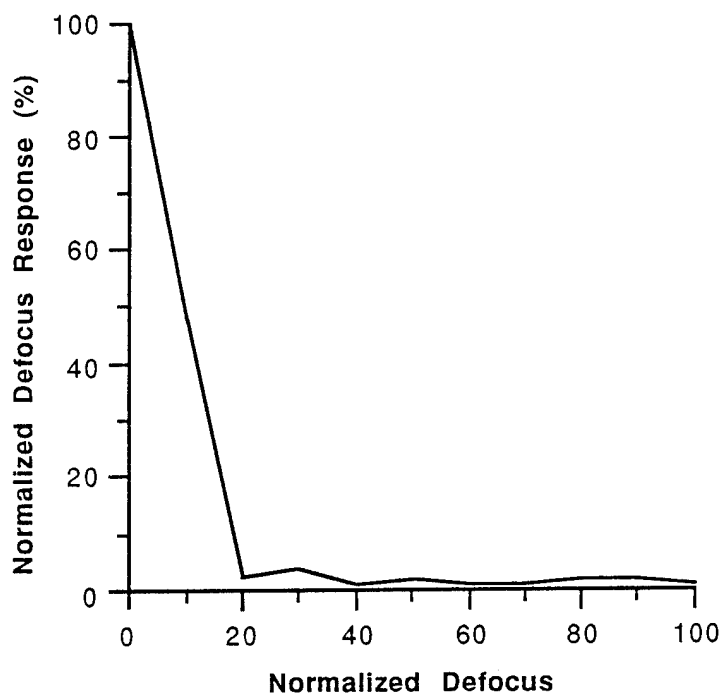


Figure 6
The defocus response of a pixel filter. $b/a = 0.5$. Microlens size = 5 times Airy spot size.

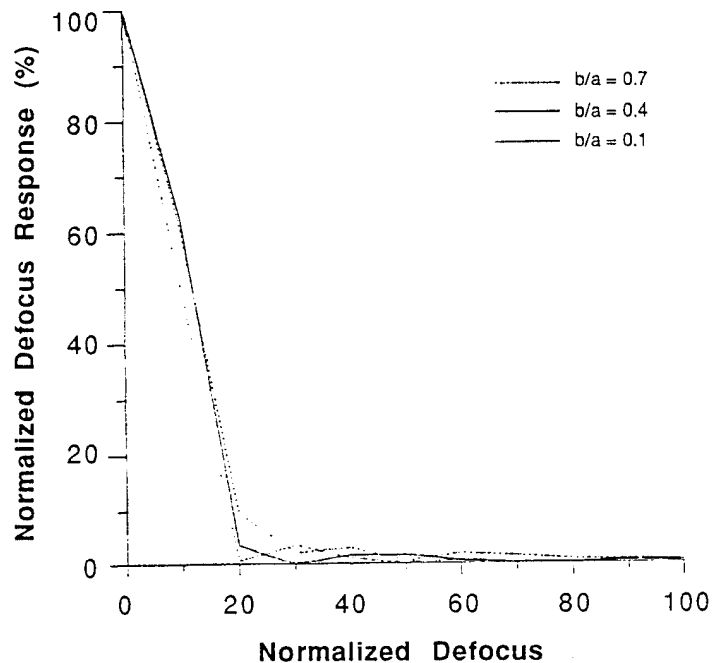


Figure 7
Defocus response for various values of central obstruction ratio b/a
(microlens size is equal to ten times Airy spot size).

3.0 DEPTH DISCRIMINATION CAPABILITIES WITHOUT WAVEFRONT MATCHED FILTERS

We also evaluated the defocus response without a wavefront matched filter. In this case, the microlens size is equal to the Airy spot size. Figure 8 shows the calculated defocus response curve. Its depth discrimination contrast is about five, much lower than that with wavefront matched filters. In comparison with conventional imaging systems, however it still demonstrates substantial depth discrimination capability.

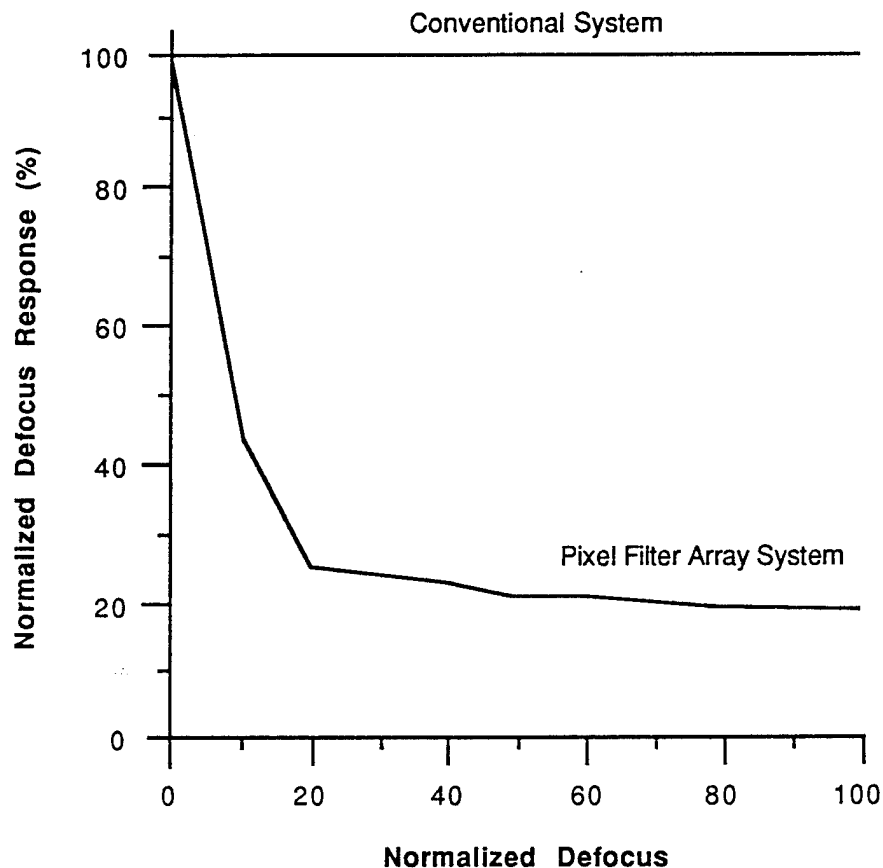


Figure 8
The defocus response without wavefront matched filters
($b/a = 0.5$, microlens size = Airy spot size).

4.0 ABERRATION EFFECTS

The effects of the imaging lens were evaluated. We added a spherical aberration factor into Eq. (3) and expressed the field diffraction by the imaging lens by

$$w(u, v) = \int_{b/a}^1 J_0(v \cdot \rho) \exp\left(j u \frac{\rho^2}{2}\right) \exp(j 2 \pi g \rho^4) \rho d \rho, \quad (10)$$

where g is the spherical aberration coefficient ($g = 1$ corresponds to one wave of spherical aberration). Figure 9 shows the defocus response curves for various values of g . They indicate that when the spherical aberration is smaller than $\lambda/4$ no significant degradation of the defocus response is generated. When g is greater than $\lambda/4$, however, depth discrimination contrast is significantly degraded. The calculations above did not employ wavefront matched filters.

When using wavefront matched filters, the effect is even worse. Figures 10(a) and (b) are for the spherical aberration coefficient $g = 0$ and $g = 1$, respectively. They show that the depth discrimination capability is significantly degraded by the aberration.

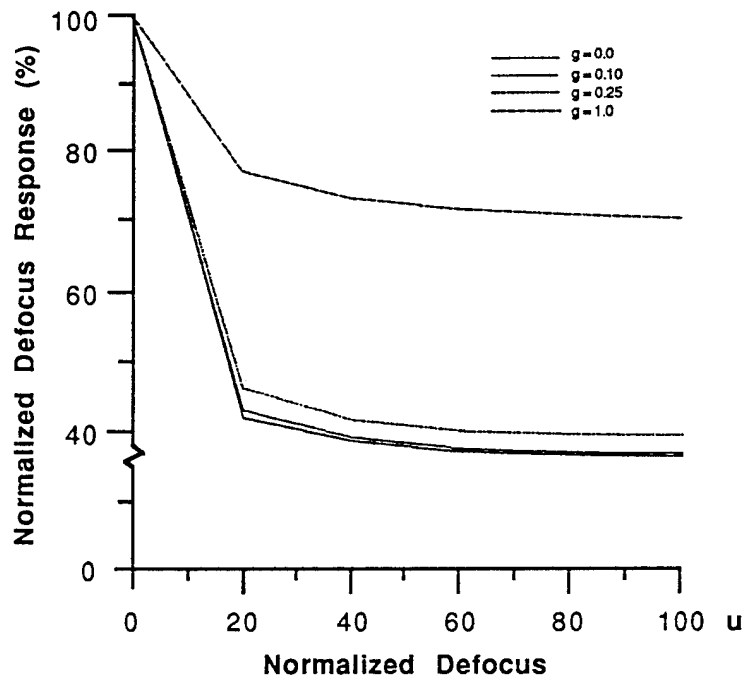
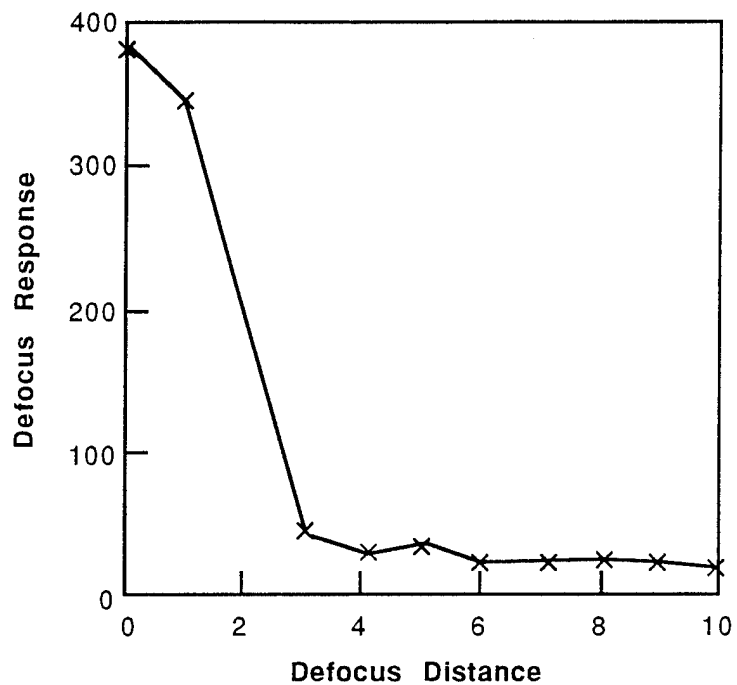
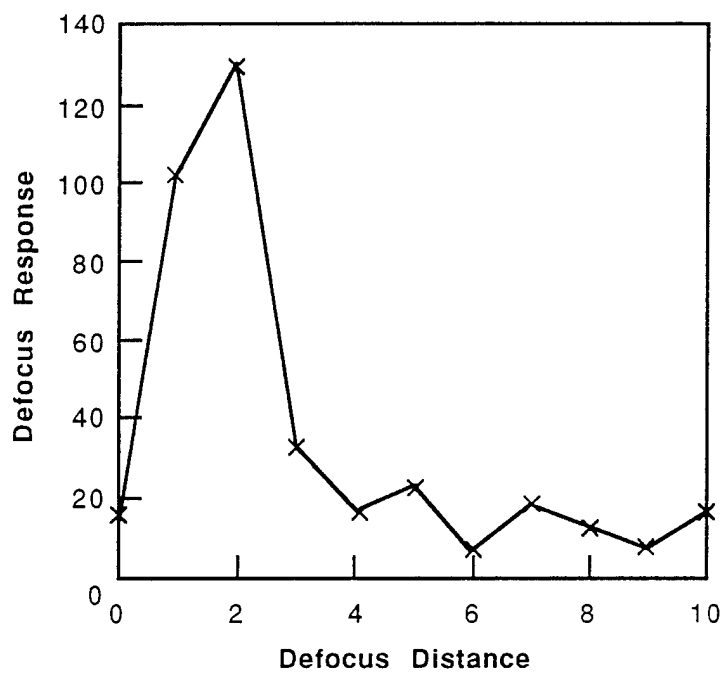


Figure 9
The aberration effects on the defocus response (without use of wavefront matched filters).



(a)

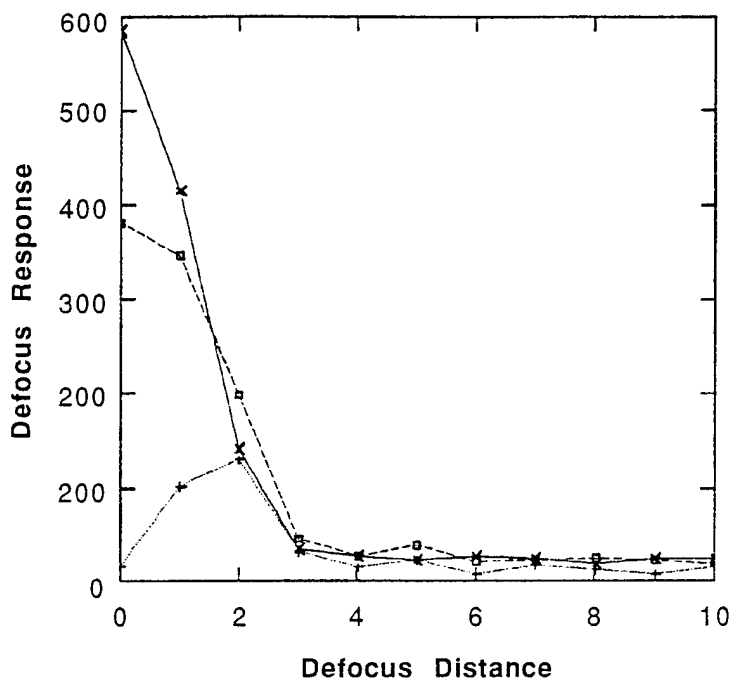


(b)

Figure 10
Aberration effects on defocus response using wavefront matched filters (a) $g=0$, (b) $g=1$.

5.0 EFFECTS OF WAVELENGTH VARIATIONS

As discussed in Section 2.0, the wavefront matched filters should match the diffraction pattern because the size of the diffraction pattern is linearly dependent on wavelength. Thus, in principle the wavefront matched filters can only match the diffraction pattern at the defocus wavelength. Figure 11 shows the effects of the wavefront variations on the defocus response. The curve marked "x" shows the defocus response for the design wavelength, λ_0 , that with " \square " is for $\lambda = 0.9\lambda_0$ and that with "+" $\lambda = 0.8\lambda_0$. They show that wavelength variation may severely deteriorate depth discrimination capability.



(a)

Figure 11
Wavelength variation effects on the defocus response.
"x" $\lambda = \lambda_0$ (design wavelength, " \square " $\lambda = 0.90 \lambda_0$, "+" $\lambda = 0.80 \lambda_0$.

In the coming months, POC will further evaluate the performance of the pixel filter technique and prepare the experimental demonstration. In preparation for commercialization, POC is discussing with a tractor manufacturer, John Deere, the industrial applications of this 3-D measurement

technique. John Deere needs a dynamic 3-dimensional deformation measurement instrument, and POC is considering proposing and developing a system for their application.